Open Ceramics 1 (2020) 100002

Contents lists available at ScienceDirect

Open Ceramics

journal homepage: www.editorialmanager.com/oceram

Ceramic-based thermoelectric generator processed via spray-coating and laser structuring

Mario Wolf [a,*], Marvin Abt [b,**], Gerd Hoffmann [c], Ludger Overmeyer [b,c], Armin Feldhoff [a,***]

[a] Institute of Physical Chemistry and Electrochemistry, Leibniz University Hannover, Callinstraße 3A, D-30167, Hannover, Germany
[b] Institute for Integrated Production Hannover, Hollerithallee 6, D-30419, Hannover, Germany
[c] Institute of Transport and Automation Technology, An der Universität 2, D-30823, Garbsen, Germany

ARTICLE INFO

Keywords:
Thermoelectric generator
Processing
Laser structuring

ABSTRACT

Processing technology to improve the manufacturing of thermoelectric generators (TEGs) is a growing field of research. In this paper, an adaptable and scalable process comprising spray-coating and laser structuring for fast and easy TEG manufacturing is presented. The developed process combines additive and subtractive processing technology towards an adaptable ceramic-based TEG, which is applicable at high temperatures and shows a high optimization potential. As a prototype, a TEG based on $Ca_3Co_4O_9$ (CCO) and Ag on a ceramic substrate was prepared. Microstructural and thermoelectric characterization is shown, reaching up to 1.65 μW cm^{-2} at 673 K and a ΔT of 100 K. The high controllability of the developed process also enables adaptation for different kinds of thermoelectric materials.

1. Introduction

Thermoelectric energy conversion has attracted researchers from various fields in recent years due to its potential in direct energy conversion from waste heat to electrical energy [1,2]. Therefore, energy harvesting of wasted thermal energy is the focus of research for several new technologies such as sensor technology and sensor networks or microelectronic devices, as well as multiple high temperature applications [3]. The energy conversion in thermoelectric materials is based on the coupling of electrical current I_{el} and entropy current I_S. When a voltage U and a temperature difference ΔT are applied across the length l of a thermoelectric materials with a cross-sectional area A, the coupled currents can be obtained for steady-state conditions by Eq. (1) [4,5]. Here, the thermoelectric material is represented by a tensor, which contains the isothermal electrical conductivity σ, the Seebeck coefficient α and the electrically open-circuited entropy conductivity Λ_{OC}.

$$\begin{pmatrix} I_{el} \\ I_S \end{pmatrix} = \frac{A}{l} \begin{pmatrix} \sigma & \sigma \cdot \alpha \\ \sigma \cdot \alpha & \sigma \cdot \alpha^2 + \Lambda_{OC} \end{pmatrix} \cdot \begin{pmatrix} U \\ \Delta T \end{pmatrix} \quad (1)$$

Note, that the here used entropy conductivity Λ_{OC} is a more fundamental parameter to describe the thermal conductivity and is connected to the traditional heat conductivity λ_{OC} via the absolute temperature T [6]. Based on this, the power factor PF of a thermoelectric material can be determined as a function of the isothermal electrical conductivity σ and the Seebeck coefficient α (Eq. (2)):

$$PF = \sigma \cdot \alpha^2 \quad (2)$$

The figure-of-merit zT (Eq. (3)), which is related to the material's power conversion efficiency, is obtained as a function of the power factor PF and the entropy conductivity Λ_{OC}.

$$zT = \frac{PF}{\Lambda_{OC}} = \frac{PF}{\lambda_{OC}} \cdot T \quad (3)$$

The basic working principle of a thermoelectric generator (TEG) via coupled currents is schematically shown in Fig. 1. Driven by the temperature difference ΔT, entropy flows from the hot side (top) to the cold side (bottom) through the device. In the alternating n- ($\alpha < 0$) and p-type ($\alpha > 0$) materials, a current of charge in the opposite or the same direction is induced, respectively. Consequently, a circular electrical current results in the case of an electrical closed circuit. As a result, a transfer from thermal energy (red arrows in Fig. 1b) to electrical energy (blue arrows in Fig. 1b) within the thermoelectric materials occurs, which can

* Corresponding author.
** Corresponding author.
*** Corresponding author.
E-mail addresses: mario.wolf@pci.uni-hannover.de (M. Wolf), abt@iph-hannover.de (M. Abt), armin.feldhoff@pci.uni-hannover.de (A. Feldhoff).

https://doi.org/10.1016/j.oceram.2020.100002
Received 18 February 2020; Received in revised form 29 April 2020; Accepted 29 April 2020
Available online 13 May 2020

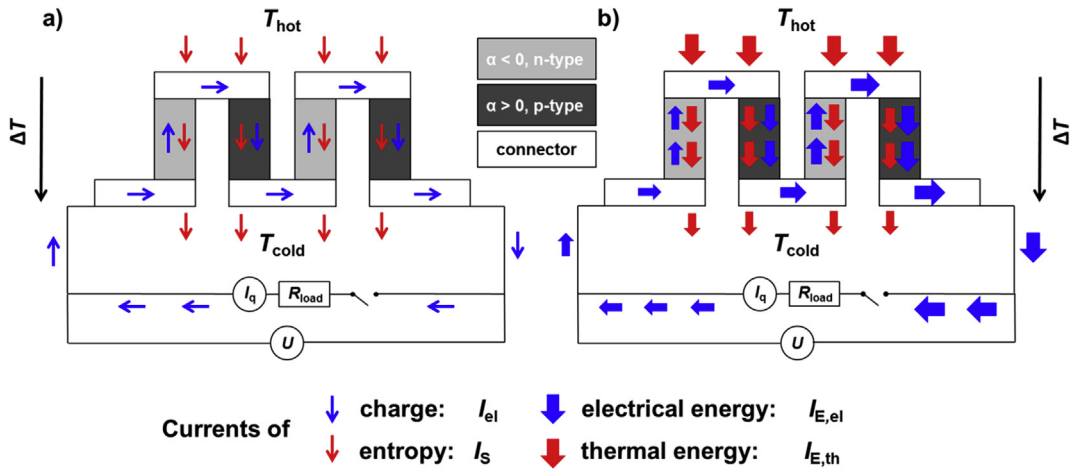

Fig. 1. Working principle schematic of a TEG with two thermocouples of *n*-type ($\alpha < 0$) and *p*-type ($\alpha > 0$) materials. a) The currents of charge I_{el} and entropy I_s are coupled in the thermoelectric materials. Entropy enters the device at the hot side (top) and leaves it at the cold side (bottom), as indicated by red arrows. The thermally induced currents of charge in the *n*-type and *p*-type materials lead to an external ring circuit, as indicated by blue arrows. Note, that the dissipation of excess entropy has been skipped for clarity. b) Thermal energy, as indicated by red arrows, enters the device at the hot side, and in the thermoelectric materials, it is partly converted into electrical energy. The latter is indicated by blue arrows. Note that the width of the blue arrows indicates that at the electrical input of the device the electrical power is low, whereas at the electrical output, it is high. The difference is the useful electrical power to drive some external load, which is symbolized by an external load resistance. (For interpretation of the references to colour in this figure legend, the reader is referred to the Web version of this article.)

be used in an external load. The electrical power output is determined by the power factor *PF* of the thermoelectric materials and the temperature difference ΔT [7].

Thermoelectric materials are therefore desired to have a high power factor *PF* and a simultaneously low open-circuited entropy conductivity Λ_{OC}. Commercially available TEGs are based on *n*- and *p*-type doped Bi_2Te_3, which provides good thermoelectric properties at room temperature [8]. However, Bi_2Te_3 struggles on its poor temperature stability and toxic precursors. Therefore, especially for application at higher temperatures [9], intermetallics such as Zintl phases [10–13] and half-Heusler phases [14–16] as well as oxide-based ceramics [17], such as layered cobaltites [18,19] or oxyselenides [20–22], have been studied extensively in the last decade. Here, the oxide-based materials are characterized by their good temperature stability in air and are less toxic compared to telluride based alternatives [9,23]. Within this group, the layered misfit $Ca_3Co_4O_9$ (CCO) is one of the best known *p*-type materials [24,25]. To further improve the material properties, many different strategies have been investigated, including doping, nanostructuring, optimization of calcination and sintering and preparation of thin films and hybrid materials [26–28].

In addition to material improvement, research has also focused on the production technology of TEGs [29]. Conventionally, TEGs are processed via manual assembling of thermoelectric materials on rigid substrates such as Al_2O_3. However, this leads to an inflexible design and a rather costly manufacturing with a noteworthy share in the overall price [29,30]. Consequently, different highly controllable and scalable manufacturing methods are the focus of research [31]. Especially, the concept of flexible thermoelectric devices via printing and additive manufacturing have been investigated recently, including various techniques such as ink jetting [32], dispensing [33,34] and screen printing [35,36]. Here, mostly organic electronics [37,38] or the conventional Bi_2Te_3 [39,40] have been investigated as thermoelectric materials. A desired high-temperature application of TEGs, however, leads to special requirements in the temperature stability and longevity of the used thermoelectric materials as well as the connectors and substrates. The above-mentioned substrate-based scalable production technologies were shown only on glass or polymeric substrates and are mostly based on organic electronics, resulting in a relatively low temperature stability, which limits the application to temperatures below 600 K [41]. For high application temperatures, only free-standing films such as flexible graphene oxide have been presented [42]. As a result, a universal and scalable preparation technique for TEGs, especially including a flexible substrate, combined with possible application at high temperatures in air is still desired.

In our previous work [43], the processing of ceramic materials such as CCO within a precisely controllable and adaptable process was presented. Here, we extend this process to develop a universal manufacturing route for functional and high-temperature applicable TEGs. To show the functionality of the process, a prototype based on the well-known CCO as thermoelectric materials is prepared. For electrical contact, commercially available Ag paste is used, which is also characterized by a high temperature stability. Spray-coating and laser structuring of the layers on a flexible low-temperature co-fired ceramic (LTCC) substrate are used to design the TEG prototype. The LTCC technology is in the focus of research since it found application in various fields of microelectronic devices and can be easily adapted to the preparation process and the final application [44–46]. It consists of ceramic particles, embedded in a polymeric matrix, thus ensuring the flexibility within the preparation and also allowing a simultaneous sintering process at high temperatures. The universal manufacturing process and adaptable substrates also enable similar processing for different kinds of thermoelectric materials and TEGs Additionally, the design of the TEG can be easily adapted to the desired application field, while the application temperature of the prepared TEG is not restricted by a polymeric substrate.

2. Experimental section

2.1. Generator design

If not mentioned separately, all reagents were obtained from commercial vendors at reagent purity of higher and used without further purification. CCO was purchased at CerPoTech (Tiller, Norway) and used to obtain spray-coating paste by dispersing 30 wt% in isopropyl alcohol via stirring and ultrasonication. As a contact material, a commercial Ag paste (conductive silver varnish spray, purchased at Tifoo) was used, because of the high temperature stability of Ag allowing the post-process sintering at 1033 K. Both pastes were applied on a commercially available two-layer flexible LTCC substrate (951 X, purchased at DuPont) with an effective substrate thickness of 440 μm via spray-coating (Sogolee Airbrush HP-200) of CCO on one side of the substrate and Ag on the other

Table 1
Details of the spray-coating process step to build CCO and Ag layers on the LTCC substrate and the laser structuring process step for partly ablation.

Spray-coating Sogolee Airbrush HP-200		Laser structuring Epilog Fusion 32 M2 Dual CO_2	
nuzzle diameter	0.2 mm	spot diameter	80 µm
pressure	3.5 bar	max. laser output	40 W
distance to substrate	30 mm	power output used	30–40%
spray-coating angle	30°	number of cycles	1
line distance	25 mm	wave type	continuous wave
number of cycles	5	scan mode	parallel line scan
subsequently dried at	373 K	scan speed	240 mm s^{-1}

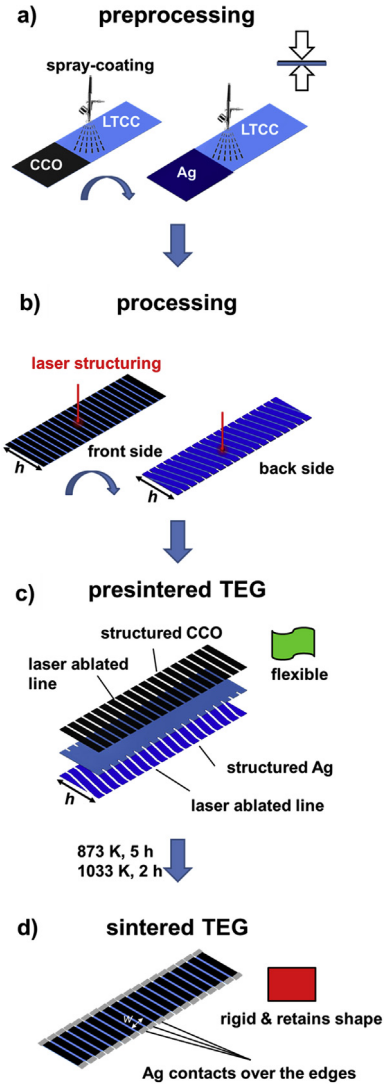

Fig. 2. Schematic manufacturing process of the TEG with CCO and Ag via a) spray-coating (preprocessing) and b) laser structuring (processing) on top of a flexible LTCC substrate. In the postprocessing step (c,d), the flexible and structured substrate is sintered to obtain a robust body. For details of the respective process parameters compare Table 1.

side. Details of the spray-coating step are shown in Table 1. The coated substrate was dried at 373 K on a heating plate after each step. A CO_2 laser (Epilog Fusion 32 M2 Dual) was used for subsequent laser structuring of both sides, details for the laser structuring are also shown in Table 1.

Subsequently, the still flexible substrate with CCO and Ag structures on the front and back side, respectively, was sintered at 873 K for 5 h and 1033 K for 2 h under air with a heating and cooling rate of 3 K min^{-1}. The maximum sintering temperature of 1033 K was chosen as a result of the commercial sintering temperature of the LTCC (1033 K) and the temperature stability of CCO, which starts to decompose above 1073 K. Finally, the CCO and Ag layers were contacted via Ag paste and again dried at 973 K for 5 h with a heating and cooling rate of 3 K min^{-1}. The developed preparation process is also shown in Fig. 2.

2.2. Microstructural characterization

Spray-coated structures and the LTCC substrate were characterized by X-ray diffraction (XRD, Bruker D8 Advance with Cu-K_α radiation). Microstructural characterization was performed with a field-emission scanning electron microscope (FE-SEM, JEOL JSM-6700F) and a field-emission transmission electron microscope (FE-TEM, JEOL JEM-2100F-UHR) both equipped with an energy-dispersive X-ray spectrometer (EDXS, Oxford Instruments INCA) for elemental analysis. The TEM was also equipped with a spectrometer for electron energy-loss spectroscopy (EELS, Gatan Imaging Filter GIF 2001). EELS measurements of the sample were carried out in scanning transmission electron microscope (STEM) mode at 0.5 eV/channel or 0.1 eV/channel with the electrostatic drift tube calibrated to the first maximum of the Ni-L_3 edge of an NiO standard (853 eV [47]). The background was subtracted with a power-law model. TEM specimen was prepared by cutting (Diamond wire saw, O'Well model 3242), infiltration with epoxy resin, grinding and polishing from both sides on polymer embedded diamond lapping films (Allied High Tech, Multiprep) down to 10 µm thickness. Subsequent Ar ion polishing (Gatan model 691 PIPS, precision ion polishing system) yielded electron transparent regions. However, for SEM analysis, fractured samples were used to prevent the porous layer to be infiltrated by epoxy resin, which would change the sample structure at the top of the porous layer.

2.3. Thermoelectric characterization

The Seebeck coefficient α and generator power output were measured as a function of the temperature with a ProboStat A setup from NorECs with ELITE thermal system and KEITHLEY 2100 Digit Multimeters. The isothermal electrical conductivity σ was measured with a home-made modified measurement cell based on the description of Indris [48] with a horizontal Carbolite tube furnace and KEITHLEY 2100 Digit Multimeters. The power factor *PF* of CCO and Ag was calculated according to Eq. (2). The power output of the generator was measured near room temperature (T_{hot} = 373 K and T_{hot} = 423 K) and at higher temperatures (T_{hot} = 573 K and T_{hot} = 673 K). For the U-I_{el} and power output curves, linear fits and second-degree polynominal fits were used, respectively. The maximum electrical power output of the TEG $P_{el,max,TEG}$ was calculated via Eq. (4) with the open-circuited voltage U_{OC} and the internal generator resistance R_{TEG} [7,38].

$$P_{el,\max,TEG} = \frac{U_{OC}^2}{4 \cdot R_{TEG}} \quad (4)$$

3. Results and discussion

The schematic manufacturing process for a TEG based on CCO and Ag via spray-coating and laser structuring is shown in Fig. 2. First, the prepared CCO paste and the Ag paste are spray-coated on the front and back side of the flexible LTCC substrate, respectively. Compared to other processing technologies such as screen printing, no additives within the pastes, which may influence the resulting properties such as electrical conductivity [49], are used and the layer thickness can be precisely controlled (compare [43]). Furthermore this can be easily transferred to other particle systems and non-planar substrates or surfaces. After a drying step, laser structuring is utilized to give a defined structure of both sides as well as make cuts for later contact. Here, the CCO is ablated from the substrates in the respective lines, resulting in a thermoleg structure.

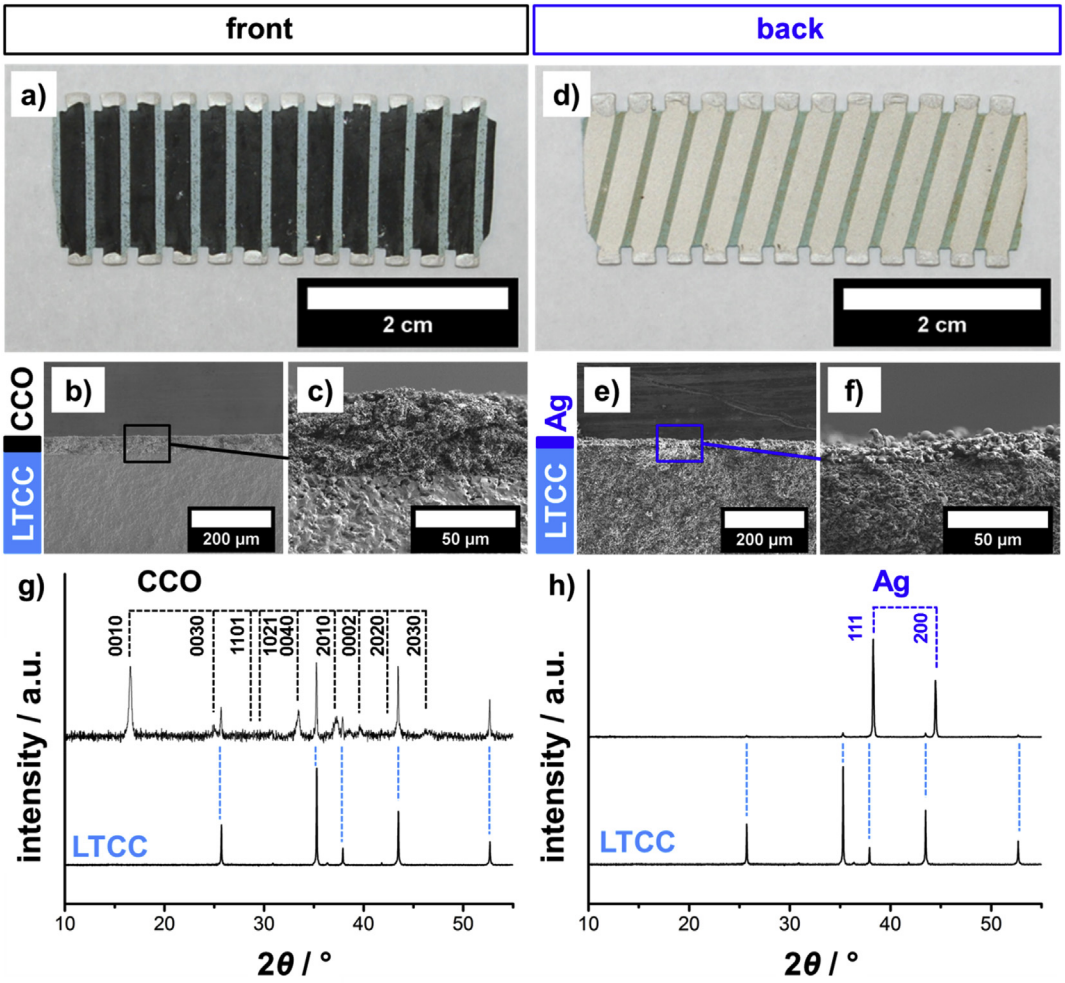

Fig. 3. Photos and SEM cross-section micrographs of the processed TEG: a,b,c) front side with CCO and d,e,f) back side with Ag. The corresponding XRD patterns confirm the presence of g) CCO and h) Ag on top of the sintered LTCC substrate. In the XRD patterns, reflections of the blank sintered LTCC substrate are given to indicate reflections from the substrate in coated specimens.

This ablation of the CCO can be done with a rather low laser power, minimizing the risk of graphit formation out of the polymeric matrix of the substrate. Accordingly, no short circuit between the resulting layers could be detected. Utilization of laser structuring enables highly controllable processing, making it possible to obtain many different structures and shapes. Additionally, compared to the established screen printing, the laser structuring does not require printing masks and is capable to reach much finer structures and therefore show a higher optimization potential. With this two-step combination of additive and subtractive processing, easy and fast preparation and structuring of large areas is enabled and the layer formation and structuring are decoupled and can be individually controlled and adapted. This is beneficial for research as well as commercial TEG manufacturing, especially due to the absence of additives and the precise control of the resulting structures. It results in a flexibility to adjust the design for a certain form or application. Subsequently, the flexible substrate and both layers are sintered at

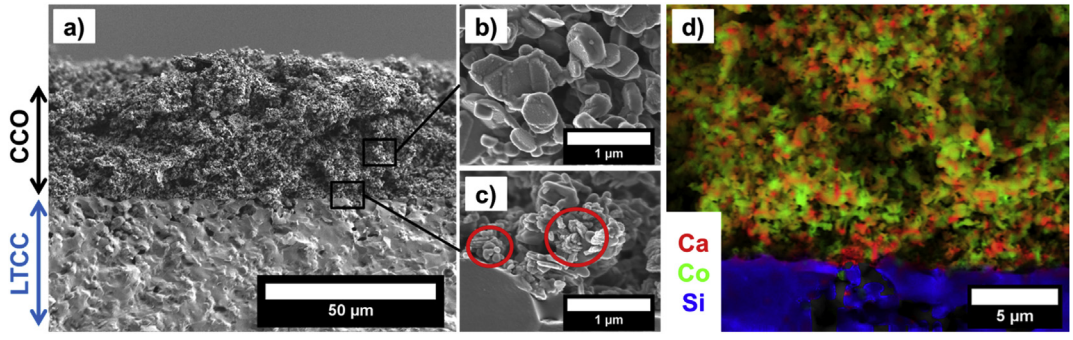

Figure 4. a-c) Cross-sectional SEM micrographs and d) EDXS elemental distribution (red: Ca, green: Co, blue: Si) of the fractured CCO-coated front side. The CCO layer shows typical platelet-like CCO crystals. EDXS elemental distribution shows the Al- and Si-based LTCC substrate and the Ca- and Co-rich phases on top. High-resolution images of the interface between the CCO layer and the LTCC substrate show smaller particles (red entangled areas in c)) attributed to the decomposition of CCO at the interface.

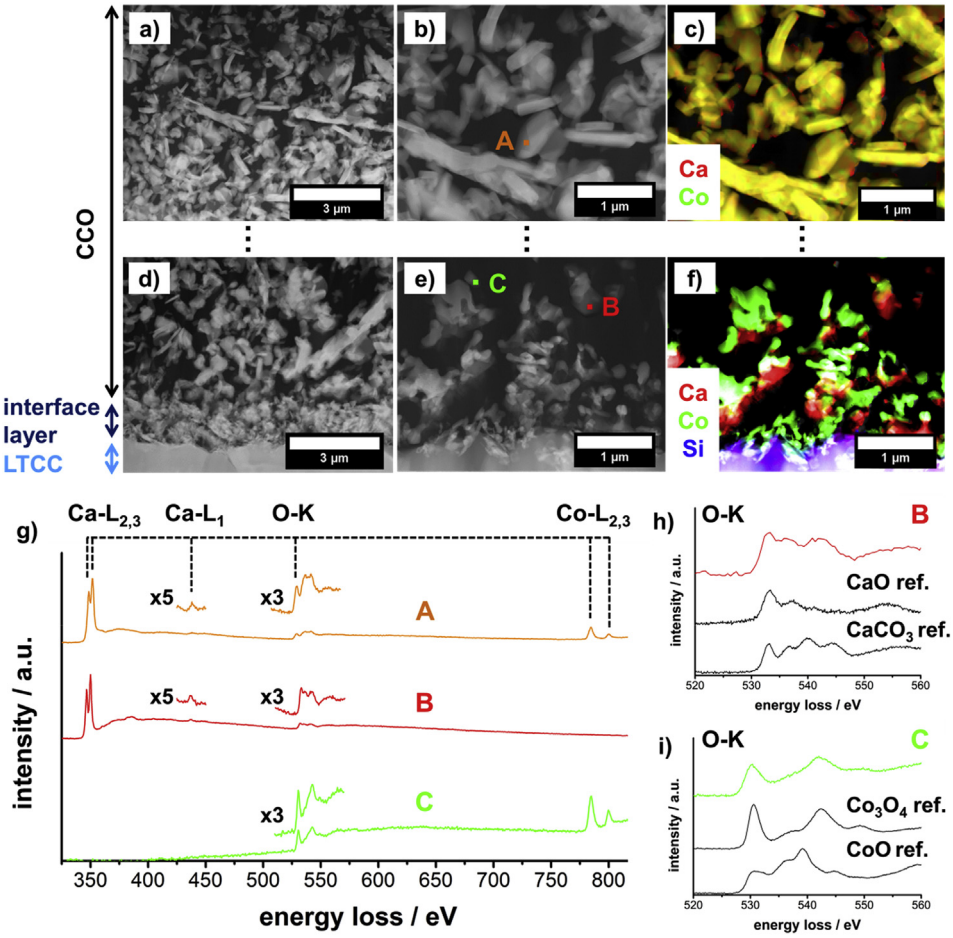

Fig. 5. Cross-sectional STEM micrographs and EDXS elemental distribution (red: Ca, green: Co, blue: Si) of the CCO coated front side a-c) in the CCO layer approximately 10 µm from the top of the substrate and d-f) at the interface of the CCO layer and the LTCC substrate. In the first 2 µm of the layer, an interface can be seen, where CCO has decomposed into Ca-rich and Co-rich phases. EELS measurements in g) of the spots marked in b) and e) proves this decomposition in the interface layer, while showing CCO above. The energy-loss near-edge structures (ELNESs) of the O–K edge in h) and i) show CaO and Ca_3O_4 as products of decomposition at the interface with the LTCC substrate. (For interpretation of the references to colour in this figure legend, the reader is referred to the Web version of this article.)

1033 K in one post-processing step resulting in a rigid TEG.

The front and back side are electrically contacted with Ag ink using the edges prepared via laser cutting. Generally, the presented process may also be adapted to various kinds of thermoelectric materials.

Micrographs of the front and back side of the resulting sintered TEG are shown in Fig. 3a and d. For this prototype, CCO structures with a width of 2 mm and a length of 20 mm have been prepared within the laser structuring process. This CCO layers on the front side are contacted via silver ink with the Ag structures on the back side. The contact can be done manually or by dipping the edges into silver ink. In the laser ablated lines, the CCO and Ag have been removed, respectively. SEM micrographs in Fig. 3b and c and Fig. 3e and f shows the corresponding layers on top of the ceramic-based LTCC substrate. The CCO layer has a layer thickness of approximately 36 µm, which can be controlled within the process via the amount of spray-coating cycles [43]. Control of the resulting layer thickness of the ceramic layer is an important parameter to adjust and improve the resulting thermoelectric properties. For this prototype, processing via 5 cycles of spray-coating, resulting in a layer thickness of approximately 36 µm, showed the best results [43]. The sintered Ag layer on the back side of the substrate exhibits a thickness of approximately 7–8 µm. XRD patterns in Fig. 3g and h confirm the presence of the CCO layer on the front side and the Ag layer on the back side of the sintered ceramic substrate, respectively.

Coatings and interfaces on both sides of the LTCC substrate were investigated in detail by SEM and EDXS elemental analysis. Fig. 4 shows the microstructural characterization of the CCO layer and its interface with the ceramic substrate. The sintered substrate mostly contains ceramic Al- and Si-based phases. Within the porous CCO layer with a thickness of approximately 36 µm, typical platelet-like CCO particles are present with diameters varying from 500 nm up to a few µm. However, at the interface of the LTCC substrate and the CCO layer, some smaller particles can be found, thus leading to the assumption of interface reactions occurring between the CCO and substrate during sintering.

Therefore, the CCO layer and especially the interface of the CCO layer and the LTCC substrate were investigated by TEM micrographs and EELS measurements, as shown in Fig. 5. Between the ceramic substrate and the CCO layer, the TEM micrographs reveal an interface layer with a thickness of approximately 2 µm. Within this interface layer, some particles smaller than the typical platelet-like CCO particles can be observed. The EDXS elemental maps (Fig. 5c and f) show that within this interface layer decomposition occurred, resulting in Ca-rich and Co-rich particles next to each other. Above this interface layer, the typical platelet-like CCO particles can be identified, and the EDXS elemental distribution also exhibits only particles containing both Ca and Co.

To further analyze the decomposition within this interface layer and to prove the identity of CCO above this layer, EELS spectra of the Ca-rich and Co-rich phases as well as of the CCO particles above were taken (Fig. 5g). While in the EELS spectra of the CCO particles, the Ca-$L_{2,3}$, O–K as well as the Co-$L_{2,3}$ edge can be observed, the particles in the interface layer exhibit only the Ca-$L_{2,3}$ or the Co-$L_{2,3}$ edge together with the O–K edge. Fine-structure measurements of the O–K edges and comparison with reference materials (Fig. 5h and i) were used to identify Co_3O_4 and CaO as products of decomposition. This corresponds to the typical decomposition products of CCO [50]. Before sintering, the LTCC substrate contains ceramic particles embedded in a polymeric matrix, while in the sintering process, the polymer is burnt out, and the ceramic particles are sintered to a rigid substrate. Here, the burn of the polymer is assumed to lead to a reduced partial oxygen pressure at the interface,

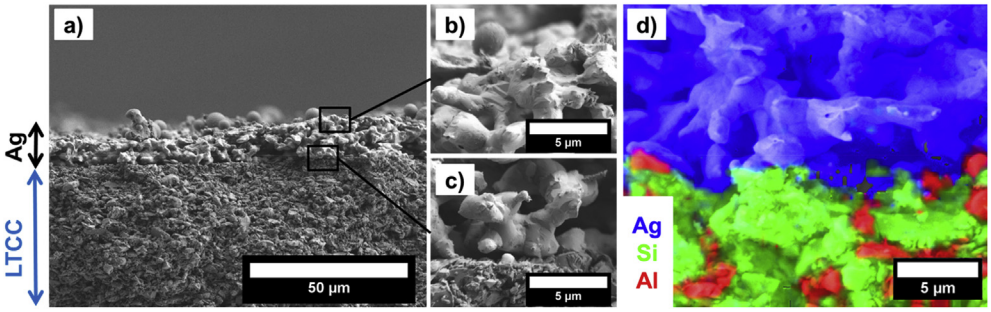

Figure 6. a-c) Cross-sectional SEM micrographs and d) EDXS elemental distribution (red: Al, green: Si, blue: Ag) of the fractured Ag-coated back side. The EDXS elemental distribution shows the Al- and Si-based LTCC substrate and the Ag layer on top.

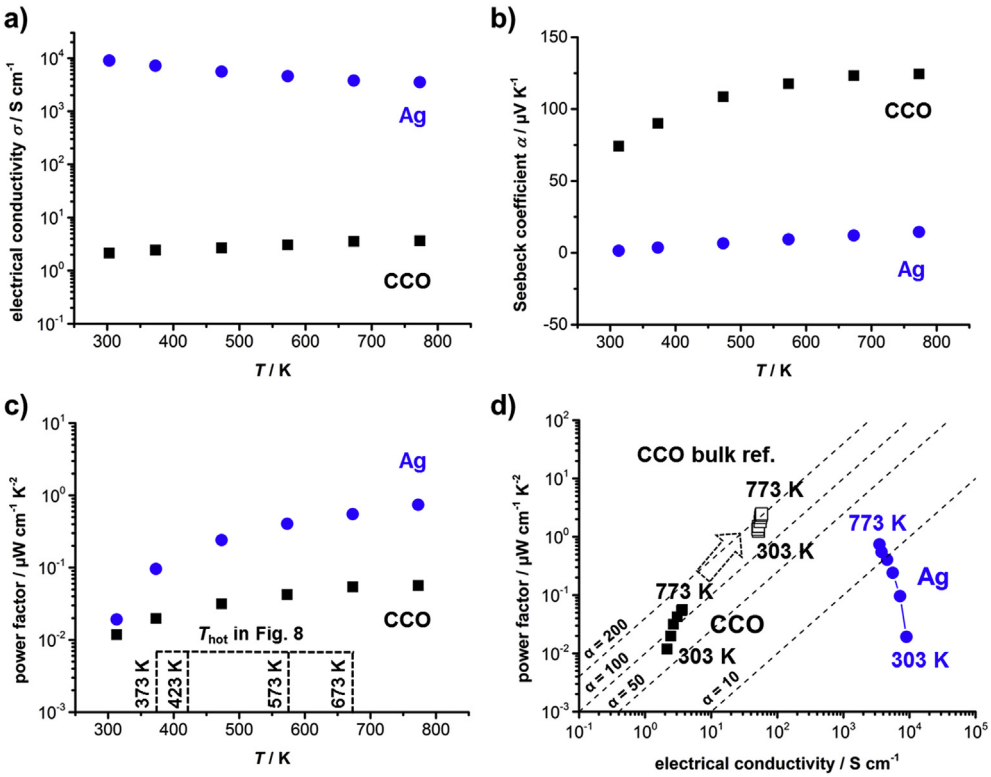

Fig. 7. Measured values of the a) electrical conductivity σ, b) Seebeck coefficient α and c) resulting power factor and d) power factor as a function of electrical conductivity (Ioffe plot) of the Ag and CCO layers. The CCO bulk reference (open symbols) [24] in d) shows an example of an achievable power factor by optimizing the CCO processing. Dashed lines in d) show the Seebeck coefficient α in µV K^{-1}.

resulting in the decomposition of the oxygen-rich CCO near the substrate and therefore the formation of cobalt oxide and calcium oxide. However, above this interface layer with a thickness of about 2 µm and therefore as main part of the layer, no decomposition of CCO has occurred, resulting in a functional thermoelectric layer.

The Ag layer on the back side was also investigated via SEM micrographs and EDXS elemental distribution (Fig. 6). The observed Ag layer exhibits a layer thickness of approximately 7–8 µm with a high porosity, analogous to the CCO layer. Here, no additional phases at the interface of the LTCC substrate and the Ag layer were found. The EDXS elemental distribution shows the Si- and Al-rich LTCC substrate and the overlying pure Ag phase with a sharp distinction.

The thermoelectric properties of both the CCO and the Ag layer are shown in Fig. 7. For the CCO, processing via 5 cycles of spray-coating were chosen, based on the analysis in the previous work [43]. The sintered Ag exhibits a high electrical conductivity of approximately 7000 S cm^{-1} at 373 K and 3000 S cm^{-1} at 773 K and a typical Seebeck coefficient of approximately 3–5 µV K^{-1}. However, the CCO exhibits a rather low electrical conductivity of approximately 2–3 S cm^{-1} which corresponds to approximately 2.5–5% of the undoped bulk material [24,51,52] and annealed undoped films [53,54]. This is mainly attributed to the high porosity of the CCO layer, which results due to the fact of a missing high pressure densification within the process. Due to the utilization of the flexible LTCC substrate, only a relatively low pressure densification with $4.2 \cdot 10^6$ Pa could be applied.

The measured Seebeck coefficient α of the CCO layer up to 125 µV K^{-1} at 773 K shows *p*-type conduction and is comparabale to reported undoped thin film CCO [53,54] prepared via chemical solution deposition and is therefore in good agreement with literature data as well as our previous results [43]. However, it is lower than that of undoped bulk CCO [24,51,52] and that of thin film CCO prepared via pulsed-laser deposition [28,55]. The resulting values of the power factor of both layers are as high as 0.06 µV cm^{-1} K^{-2} and as high as 0.75 µW cm^{-1} K^{-2} for the CCO and Ag layers at 773 K, respectively. To allow an easy comparison of measured data with literature, Fig. 7d summarizes the measured thermoelectric properties of both layers in an Ioffe plot,

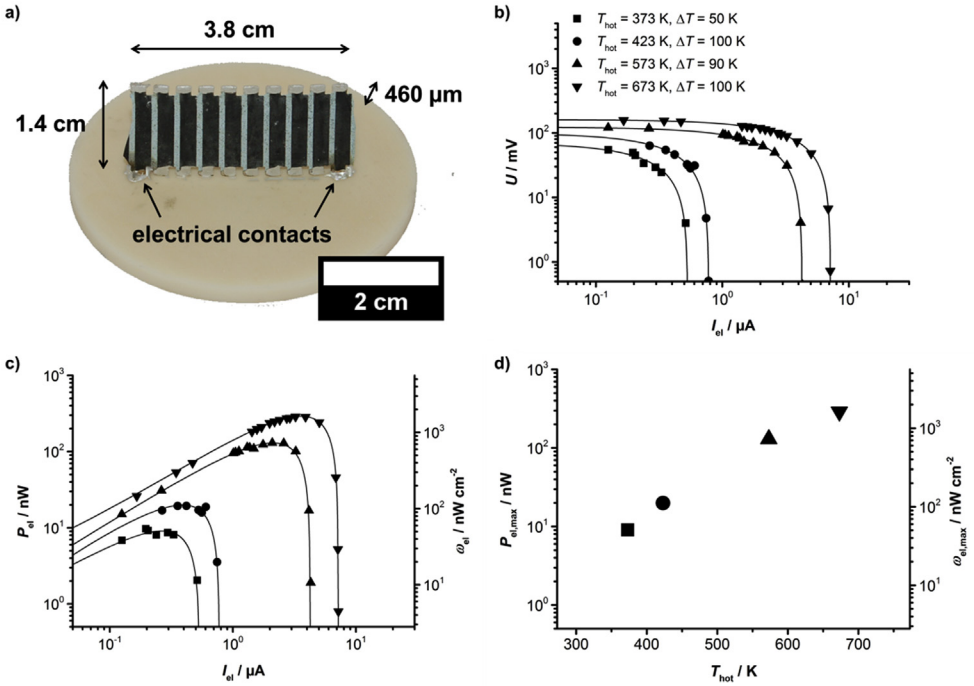

Fig. 8. a) Photograph of the prototype TEG (10 CCO and 9 Ag layers) with a length of 3.8 cm and a thickness of 460 µm. Note that the temperature gradient is applied from the top to the bottom, resulting in an effective area of 0.175 cm^2. b) Voltage and c) electrical power output P_{el} and electrical power density ω_{el} as a function of the electrical current I_{el} measured at T_{hot} = 373 K and $\Delta T \approx 50$ K, T_{hot} = 423 K and $\Delta T \approx 100$ K, T_{hot} = 573 K and $\Delta T \approx 90$ K and T_{hot} = 673 K and $\Delta T \approx 100$ K. Data in d) show the correspodning $P_{el,max}$ and $\omega_{el,max}$ as a function of T_{hot}.

Table 2
Measure values of the open-circuited voltage U_{OC} and short-circuited electrical current $I_{el,SC}$ and via Eq. (4) calculated maximum electrical power output $P_{el,max}$ of the TEG at different applied T_{hot}. The electrical power density $\omega_{el,max}$ was obtained by normalizing the maximum electrical power output $P_{el,max}$ with the geometry shown in Fig. 8a.

T_{hot}/K	ΔT/K	U_{OC}/mV	$I_{el,SC}$/mA	$P_{el,max}$/nW	$\omega_{el,max}$/nW cm^{-2}
373	50	70.5	$5.28 \cdot 10^{-4}$	9.31	53.18
423	100	99.7	$7.82 \cdot 10^{-4}$	19.49	111.38
573	90	122.96	$4.14 \cdot 10^{-3}$	127.26	727.20
673	100	161.16	$7.18 \cdot 10^{-3}$	289.28	1653.03

showing the power factor as a function of the electrical conductivity. Displayed reference data for undoped bulk CCO [24] show the potential of optimizing the CCO processing, especially by gaining higher densification and therefore less porosity of the CCO layer to obtain a higher power factor. For this, the process may be transferred to other kinds of thermoelectric materials or performed on alternative substrates, where a high pressure densification step can be done or is not even needed. Note also, that for this prototype, undoped CCO has been used, to prove the functionality of the system. As a result, the thermoelectric properties could also be enhanced by using doped CCO or hybrid materials e.g. Ag-added CCO.

In Fig. 8, the voltage-electrical current curves and the resulting electrical power output of the prepared prototype TEG at different T_{hot} values are given. At relatively low temperatures, the device reaches $P_{el,max}$ = 10 and 20 nW at a ΔT of approximately 50 K and 100 K, respectively. With the geometry of 0.175 cm^2, shown in Fig. 8a, this corresponds to an electrical power density $\omega_{el,max}$ of 50–115 nW cm^{-2}. Both the electrical conductivity σ and the Seebeck coefficient α of both sides increase with increasing temperature, resulting in an analogous increase in the electrical power output of the generator. At T_{hot} = 673 K and ΔT = 100 K, the processed TEG reaches an electrical power output of $P_{el,max}$ = 289 nW and a corresponding electrical power density of $\omega_{el,max}$ of 1.65 µW cm^{-2}.

Table 2 summarizes the measured thermoelectric parameters at different applied temperature conditions. With an electrical power density of 1.65 µW cm^{-2} with 10 CCO and 9 Ag layers, this prototype provide similar electrical power density compared to printed devices based on thermoelectric polymers, which are usually in the range of approximately 500 nm [56,57] up to several µW with a high amount of thermocouples [58]. However, Bi_2Te_3-based printed devices have been reported to reach higher electrical power densities, e.g. by Chen et al. [59] up to 75 µW cm^{-2} at a ΔT of 20 K or by Kim et al. [60] reaching 3.8 mW cm^{-2} at a ΔT of 50 K. Compared to this, our prototype provides a rather low electrical power density, which is attributed to the low electrical conductivity of the CCO layer, resulting in a high electrical resistivity of the generator R_{TEG}. Further adjustment of the presented process, especially the sintering of the layers and of course the adaptation to other thermoelectric materials, may strongly increase the electrical power output of the processed generator, making the presented manufacturing process a promising way to prepare and adapt TEGs for a desired application.

4. Conclusions

An adaptable process for TEG manufacturing has been presented on the example of a prototype based on CCO and Ag on a ceramic-based LTCC substrate. The structure and shape of the thermoelectric layers and the resulting TEG are given by the utilization of spray-coating and laser structuring, while no printing masks or additives are required. The prepared prototype consists of porous layers of CCO and Ag and is applicable at higher temperature compared to polymer-based manufactured TEGs. An electrical power density of up to 1.65 µW cm^{-2} at 673 K and a ΔT of 100 K could be achieved, mainly limited by the high porosity of the ceramic CCO layer reaching a low electrical conductivity of only approximately 5% of the bulk material. However, a high potential to optimize the thermoelectric properties and electrical power output is given by adjusting the process to tailor the densification and sintering of the layers and further adjustment of the thermoelectric materials. The presented process may also be adapted to different kinds of thermoelectric materials and TEG design for various applications.

Declaration of competing interest

The authors declare that they have no known competing financial interests or personal relationships that could have appeared to influence

the work reported in this paper.

Acknowledgment

This work was funded by the Deutsche Forschungsgemeinschaft (DFG, German Research Foundation) – project number 325156807. The publication of this article was funded by the Open Access Fund of Leibniz Universität Hannover.

References

[1] G.J. Snyder, E.S. Toberer, Complex thermoelectric materials, Nat. Mater. 7 (2008) 105–114, https://doi.org/10.1038/nmat2090.
[2] J. He, T.M. Tritt, Advances in thermoelectric materials research: Looking back and Moving Forward, Science 80 (2017) 357, https://doi.org/10.1126/SCIENCE.AAK9997, eaak9997.
[3] R.A. Kishore, A. Marin, C. Wu, A. Kumar, S. Priya, Energy Harvesting - Materials, Physics, and System Design with Practical Examples, DEStech Publications, 2019.
[4] H.U. Fuchs, The Dynamics of Heat - A Unified Approach to Thermodynamics and Heat Transfer, 2nd ed., Springer-Verlag, New York, 2010 https://doi.org/10.1007/978-1-4419-7604-8.
[5] A. Feldhoff, Thermoelectric material tensor Derived from the Onsager–de Groot–Callen model, Energy Harvest. Syst. 2 (2015) 5–13, https://doi.org/10.1515/ehs-2014-0040.
[6] M. Wolf, K. Menekse, A. Mundstock, R. Hinterding, F. Nietschke, O. Oeckler, A. Feldhoff, Low thermal conductivity in thermoelectric oxide-based Multiphase Composites, J. Electron. Mater. 48 (2019) 7551–7561, https://doi.org/10.1007/s11664-019-07555-2.
[7] M. Bittner, N. Kanas, R. Hinterding, F. Steinbach, J. Räthel, M. Schrade, K. Wiik, M. Einarsrud, A. Feldhoff, A Comprehensive Study on improved power materials for high-temperature thermoelectric generators, J. Power Sources 410–411 (2019) 143–151, https://doi.org/10.1016/j.jpowsour.2018.10.076.
[8] H. Mamur, M.R.A. Bhuiyan, F. Korkmaz, M. Nil, A Review on Bismuth telluride (Bi_2Te_3) nanostructure for thermoelectric applications, Renew. Sustain. Energy Rev. 82 (2018) 4159–4169, https://doi.org/10.1016/j.rser.2017.10.112.
[9] M. Wolf, R. Hinterding, A. Feldhoff, High power factor vs . High zT — a Review of thermoelectric materials for high-temperature application, Entropy 21 (2019) 1058, https://doi.org/10.3390/e21111058.
[10] J. Shuai, J. Mao, S. Song, Q. Zhang, G. Chen, Z. Ren, Recent Progress and Future Challenges on thermoelectric Zintl materials, Mater. Today Phys. 1 (2017) 74–95, https://doi.org/10.1016/j.mtphys.2017.06.003.
[11] J.H. Grebenkemper, S. Klemenz, B. Albert, S.K. Bux, S.M. Kauzlarich, Effects of Sc and Y Substitution on the structure and thermoelectric properties of $Yb_{14}MnSb_{11}$, J. Solid State Chem. 242 (2016) 55–61, https://doi.org/10.1016/j.jssc.2016.03.015.
[12] P. Gorai, B.R. Ortiz, E.S. Toberer, V. Stevanović, Investigation of n-type doping strategies for Mg_3Sb_2, J. Mater. Chem. A. 6 (2018) 13806–13815, https://doi.org/10.1039/C8TA03344G.
[13] X. Chen, H. Wu, J. Cui, Y. Xiao, Y. Zhang, J. He, Y. Chen, J. Cao, W. Cai, S.J. Pennycook, Z. Liu, L.D. Zhao, J. Sui, Extraordinary thermoelectric performance in n-type Manganese doped Mg_3Sb_2 Zintl: high Band Degeneracy, Tuned carrier Scattering Mechanism and Hierarchical microstructure, Nano Energy 52 (2018) 246–255, https://doi.org/10.1016/j.nanoen.2018.07.059.
[14] L. Chen, S. Gao, X. Zeng, A. Mehdizadeh Dehkordi, T.M. Tritt, S.J. Poon, Uncovering high thermoelectric figure of merit in (Hf,Zr)NiSn half-Heusler Alloys, Appl. Phys. Lett. 107 (2015), https://doi.org/10.1063/1.4927661.
[15] C. Fu, T. Zhu, Y. Liu, H. Xie, X. Zhao, Band Engineering of high performance p-type FeNbSb based half-Heusler thermoelectric materials for figure of merit $zT > 1$, Energy Environ. Sci. 8 (2015) 216–220, https://doi.org/10.1039/c4ee03042g.
[16] H. Zhu, R. He, J. Mao, Q. Zhu, C. Li, J. Sun, W. Ren, Y. Wang, Z. Liu, Z. Tang, A. Sotnikov, Z. Wang, D. Broido, D.J. Singh, G. Chen, K. Nielsch, Z. Ren, Discovery of ZrCoBi based half Heuslers with high thermoelectric conversion efficiency, Nat. Commun. 9 (2018) 1–9, https://doi.org/10.1038/s41467-018-04958-3.
[17] Y. Yin, B. Tudu, A. Tiwari, Recent Advances in oxide thermoelectric materials and Modules, Vacuum 146 (2017) 356–374, https://doi.org/10.1016/j.vacuum.2017.04.015.
[18] J.W. Fergus, Oxide materials for high temperature thermoelectric energy conversion, J. Eur. Ceram. Soc. 32 (2012) 525–540, https://doi.org/10.1016/j.jeurceramsoc.2011.10.007.
[19] M. Ohtaki, Recent Aspects of oxide thermoelectric materials for power generation from Mid-to-high temperature heat Source, J. Ceram. Soc. Japan. 119 (2011) 770–775, https://doi.org/10.2109/jcersj2.119.770.
[20] X. Zhang, C. Chang, Y. Zhou, L.D. Zhao, BiCuSeO thermoelectrics: an Update on recent Progress and Perspective, Materials 10 (2017) 1–16, https://doi.org/10.3390/ma10020198.
[21] Y. Liu, L.D. Zhao, Y. Zhu, Y. Liu, F. Li, M. Yu, D.B. Liu, W. Xu, Y.H. Lin, C.W. Nan, Synergistically optimizing electrical and thermal Transport properties of BiCuSeO via a Dual-doping Approach, Adv. Energy Mater. 6 (2016) 1–9, https://doi.org/10.1002/aenm.201502423.
[22] X. Zhang, D. Feng, J. He, L.D. Zhao, Attempting to Realize n-type BiCuSeO, J. Solid State Chem. 258 (2018) 510–516, https://doi.org/10.1016/j.jssc.2017.11.012.
[23] S. Bresch, B. Mieller, D. Schoenauer-Kamin, R. Moos, F. Giovanelli, T. Rabe, Influence of pressure Assisted sintering and reaction sintering on microstructure and thermoelectric properties of bi-doped and undoped calcium cobaltite, J. Appl. Phys. 126 (2019), https://doi.org/10.1063/1.5107476, 0–11.
[24] M. Bittner, L. Helmich, F. Nietschke, B. Geppert, O. Oeckler, A. Feldhoff, Porous $Ca_3Co_4O_9$ with enhanced thermoelectric properties Derived from Sol–Gel Synthesis, J. Eur. Ceram. Soc. 37 (2017) 3909–3915, https://doi.org/10.1016/j.jeurceramsoc.2017.04.059.
[25] S. Saini, H.S. Yaddanapudi, K. Tian, Y. Yin, D. Magginetti, A. Tiwari, Terbium ion doping in $Ca_3Co_4O_9$: a step towards high-Performance thermoelectric materials, Sci. Rep. 7 (2017) 1–9, https://doi.org/10.1038/srep44621.
[26] C. Gayner, K.K. Kar, Recent Advances in thermoelectric materials, Prog. Mater. Sci. 83 (2016) 330–382, https://doi.org/10.1016/j.pmatsci.2016.07.002.
[27] S. Bresch, B. Mieller, C. Selleng, T. Stöcker, R. Moos, T. Rabe, Influence of the calcination Procedure on the thermoelectric properties of calcium cobaltite $Ca_3Co_4O_9$, J. Electroceramics. 40 (2018) 225–234, https://doi.org/10.1007/s10832-018-0124-3.
[28] V. Rogé, F. Delorme, A. Stolz, A. Talbi, N. Semmar, J. Perrière, F. Giovannelli, E. Millon, Effect of post-deposition thermal Treatment on thermoelectric properties of pulsed-laser deposited $Ca_3Co_4O_9$ thin films, Mater. Chem. Phys. 221 (2019) 361–366, https://doi.org/10.1016/j.matchemphys.2018.09.069.
[29] R. He, G. Schierning, K. Nielsch, Thermoelectric devices: a Review of devices, Architectures, and contact optimization, Adv. Mater. Technol. 3 (2018), https://doi.org/10.1002/admt.201700256.
[30] S. Leblanc, S.K. Yee, M.L. Scullin, C. Dames, K.E. Goodson, Material and manufacturing Cost Considerations for thermoelectrics, Renew. Sustain. Energy Rev. 32 (2014) 313–327, https://doi.org/10.1016/j.rser.2013.12.030.
[31] M. Orrill, S. LeBlanc, Printed thermoelectric materials and devices: Fabrication techniques, Advantages and Challenges, J. Appl. Polym. Sci. 134 (2017) 44256, https://doi.org/10.1002/app.44256.
[32] C. Ou, A.L. Sangle, T. Chalklen, Q. Jing, V. Narayan, S. Kar-Narayan, Enhanced thermoelectric properties of flexible Aerosol-Jet printed Carbon Nanotube-based Nanocomposites, Apl. Mater. 6 (2018), 096101, https://doi.org/10.1063/1.5043547.
[33] D. Madan, A. Chen, P.K. Wright, J.W. Evans, Dispenser printed Composite thermoelectric Thick films for thermoelectric generator applications, J. Appl. Phys. 109 (2011), 034904, https://doi.org/10.1063/1.3544501.
[34] D. Madan, A. Chen, P.K. Wright, J.W. Evans, Printed Se-doped MA n-type Bi_2Te_3 Thick-film thermoelectric generators, J. Electron. Mater. 41 (2012) 1481–1486, https://doi.org/10.1007/s11664-011-1885-5.
[35] Z. Cao, E. Koukharenko, M.J. Tudor, R.N. Torah, S.P. Beeby, Flexible screen printed thermoelectric generator with enhanced Processes and materials, Sensors Actuators, A Phys. 238 (2016) 196–206, https://doi.org/10.1016/j.sna.2015.12.016.
[36] S.J. Kim, H. Choi, Y. Kim, J.H. We, J.S. Shin, H.E. Lee, M.W. Oh, K.J. Lee, B.J. Cho, Post Ionized Defect Engineering of the screen-printed $Bi_2Te_{2.7}Se_{0.3}$ Thick film for high performance flexible thermoelectric generator, Nano Energy 31 (2017) 258–263, https://doi.org/10.1016/j.nanoen.2016.11.034.
[37] Y. Chen, Y. Zhao, Z. Liang, Solution processed organic thermoelectrics: towards flexible thermoelectric Modules, Energy Environ. Sci. 8 (2015) 401–422, https://doi.org/10.1039/c4ee03297g.
[38] R. Kroon, D.A. Mengistie, D. Kiefer, J. Hynynen, J.D. Ryan, L. Yu, C. Müller, Thermoelectric Plastics: from design to Synthesis, processing and structure-Property relationships, Chem. Soc. Rev. 45 (2016) 6147–6164, https://doi.org/10.1039/c6cs00149a.
[39] Z. Cao, M.J. Tudor, R.N. Torah, S.P. Beeby, Screen printable flexible BiTe-SbTe-based Composite thermoelectric materials on Textiles for Wearable applications, IEEE Trans. Electron Devices 63 (2016) 4024–4030, https://doi.org/10.1109/TED.2016.2603071.
[40] T. Zhang, K. Li, C. Li, S. Ma, H.H. Hng, L. Wei, Mechanically durable and flexible thermoelectric films from PEDOT:PSS/PVA/$Bi_{0.5}Sb_{1.5}Te_3$ Nanocomposites, Adv. Electron. Mater. 3 (2017) 1–9, https://doi.org/10.1002/aelm.201600554.
[41] X. Liu, Z. Wang, Printable thermoelectric materials and applications, Front. Mater. 6 (2019) 1–5, https://doi.org/10.3389/fmats.2019.00088.
[42] T. Li, A.D. Pickel, Y. Yao, Y. Chen, Y. Zeng, S.D. Lacey, Y. Li, Y. Wang, J. Dai, Y. Wang, B. Yang, M.S. Fuhrer, A. Marconnet, C. Dames, D.H. Drew, L. Hu, Thermoelectric properties and performance of flexible reduced graphene oxide films up to 3,000 K, Nat. Energy. 3 (2018) 148–156, https://doi.org/10.1038/s41560-018-0086-3.
[43] M. Abt, M. Wolf, A. Feldhoff, L. Overmeyer, Combined spray-coating and laser structuring of thermoelectric ceramics, J. Mater. Process. Technol. 275 (2020) 116319, https://doi.org/10.1016/j.jmatprotec.2019.116319.
[44] M.T. Sebastian, R. Ubic, H. Jantunen, Low-loss Dielectric ceramic materials and their properties, Int. Mater. Rev. 60 (2015) 392–412, https://doi.org/10.1179/1743280415Y.0000000007.
[45] J.M. Dominik Jurków, Thomas Maeder, Arkadiusz Dąbrowski, Marina Santo Zarnik, Darko Belavič, Heike Bartsch, Overview on low temperature co-fired ceramic sensors, Sensors Actuators, A Phys. 233 (2015) 125–146, https://doi.org/10.1016/j.sna.2015.05.023.
[46] Z. Sun, W. Li, Y. Liu, H. Zhang, D. Zhu, H. Sun, C. Hu, S. Chen, Design and preparation of a Novel Degradable low-temperature co-fired ceramic (LTCC) Composites, Ceram. Int. 45 (2019) 7001, https://doi.org/10.1016/j.ceramint.2018.12.201, 7010.
[47] P.L. Potapov, D. Schryvers, Measuring the absolute Position of EELS Ionisation edges in a TEM, Ultramicroscopy 99 (2004) 73–85, https://doi.org/10.1016/S0304-3991(03)00185-2.
[48] S. Indris, Perkolation von Grenzflächen in nanokristallinen keramischen Kompositen, 1st ed., Cuvillier Verlag, Göttingen, 2001.

[49] X. Huang, T. Leng, X. Zhang, J.C. Chen, K.H. Chang, A.K. Geim, K.S. Novoselov, Z. Hu, Binder-free highly conductive graphene Laminate for low Cost printed Radio Frequency applications, Appl. Phys. Lett. 106 (2015) 203105, https://doi.org/10.1063/1.4919935.

[50] M. Sopicka-Lizer, P. Smaczyński, K. Kozłowska, E. Bobrowska-Grzesik, J. Plewa, H. Altenburg, Preparation and characterization of calcium cobaltite for thermoelectric application, J. Eur. Ceram. Soc. 25 (2005) 1997–2001, https://doi.org/10.1016/j.jeurceramsoc.2005.03.222.

[51] M.E. Song, H. Lee, M.G. Kang, W. Li, D. Maurya, B. Poudel, J. Wang, M.A. Meeker, G.A. Khodaparast, S.T. Huxtable, S. Priya, Nanoscale Texturing and interfaces in Compositionally modified $Ca_3Co_4O_9$ with enhanced thermoelectric performance, ACS Omega 3 (2018) 10798–10810, https://doi.org/10.1021/acsomega.8b01552.

[52] S. Porokhin, L. Shvanskaya, V. Khovaylo, A. Vasiliev, Effect of NaF doping on the thermoelectric properties of $Ca_3Co_4O_9$, J. Alloys Compd. 695 (2017) 2844–2849, https://doi.org/10.1016/j.jallcom.2016.11.405.

[53] R. Wei, H. Jian, X. Tang, J. Yang, L. Hu, L. Chen, J. Dai, X. Zhu, Y. Sun, Enhanced thermoelectric properties in Cu-doped c-Axis-Oriented $Ca_3Co_4O_{9+\delta}$ thin films, J. Am. Ceram. Soc. 96 (2013) 2396–2401, https://doi.org/10.1111/jace.12415.

[54] J. Buršík, M. Soroka, K. Knížek, J. Hirschner, P. Levinský, J. Hejtmánek, Oriented thin films of $Na_{0.6}CoO_2$ and $Ca_3Co_4O_9$ deposited by Spin-coating method on Polycrystalline substrate, Thin Solid Films 603 (2016) 400–403, https://doi.org/10.1016/j.tsf.2016.02.056.

[55] B. Paul, J. Lu, P. Eklund, Nanostructural tailoring to Induce flexibility in thermoelectric $Ca_3Co_4O_9$ thin films, ACS Appl. Mater. Interfaces 9 (2017) 25308–25316, https://doi.org/10.1021/acsami.7b06301.

[56] O. Bubnova, Z.U. Khan, A. Malti, S. Braun, M. Fahlman, M. Berggren, X. Crispin, Optimization of the thermoelectric figure of merit in the conducting polymer Poly(3,4-ethylenedioxythiophene), Nat. Mater. 10 (2011) 429–433, https://doi.org/10.1038/nmat3012.

[57] A. Besganz, V. Zöllmer, R. Kun, E. Pál, L. Walder, M. Busse, Inkjet printing as a flexible technology for the deposition of thermoelectric Composite structures, Procedia Technol 15 (2014) 99–106, https://doi.org/10.1016/j.protcy.2014.09.043.

[58] H. Fang, B.C. Popere, E.M. Thomas, C.-K. Mai, W.B. Chang, G.C. Bazan, M.L. Chabinyc, R.A. Segalman, Large-scale Integration of flexible materials into Rolled and Corrugated thermoelectric Modules, J. Appl. Polym. Sci. 134 (2017) 44208, https://doi.org/10.1002/app.44456.

[59] A. Chen, D. Madan, P.K. Wright, J.W. Evans, Dispenser-printed planar Thick-film thermoelectric energy generators, J. Micromechanics Microengineering. 21 (2011) 104006, https://doi.org/10.1088/0960-1317/21/10/104006.

[60] S.J. Kim, J.H. We, B.J. Cho, A Wearable thermoelectric generator Fabricated on a glass Fabric, Energy Environ. Sci. 7 (2014) 1959–1965, https://doi.org/10.1039/c4ee00242c.